Magnetic Resonance Imaging of Typical Polypoid Adenomyoma of the Uterus in 8 Patients: Correlation With Pathological Findings

Kazuhiro Kitajima, MD, Kazufumi Imanaka, MD,* Yoichiro Kuwata, MD,* Kimio Hashimoto, MD,† and Kazuro Sugimura, MD‡*

Objective: To study the magnetic resonance imaging findings of typical polypoid adenomyoma and correlate radiological findings with histopathologic findings.

Methods: Magnetic resonance imaging and histopathologic findings were retrospectively reviewed in 8 patients. The size, location, polyp's shape, and signal intensity of magnetic resonance imaging findings were evaluated.

Results: The polyp's shape of 8 cases is pedunculated in 7 and sessile in 1, and all 8 cases are well circumscribed. Four cases (50%) show an isointense mass relative to the myometrium with small or large hyperintense foci on T1-weighted imaging (T1WI) or T2-weighted imaging (T2WI), reflecting the fascicle of smooth muscle with islands of hemorrhagic endometrial tissue. One case forms a large hemorrhagic cavity, being hyperintense on T1WI and hypointense on T2WI. Three cases (37%) show almost homogeneous isointense or hyperintense mass on T2WI.

Conclusions: When there is a well-defined polypoid mass protrusion into the uterine endometrial cavity that is isointense relative to the myometrium with small or large foci of high signal on T1WI or T2WI in a premenopausal woman, typical polypoid adenomyoma can be considered in the differential diagnosis.

Key Words: uterine neoplasms, adenomyosis, MRI

(*J Comput Assist Tomogr* 2007;31:463–468)

Polypoid adenomyoma (adenomatous polyp) of the uterus is an endometrial polyp in which the stroma is predominantly composed of smooth muscle. Although it is uncommon, accounting for only 1.3% of all endometrial polyps, the frequency of detection is increasing.[1–3] It is of mixed epithelial and mesenchymal origin, with typical and atypical variant. The typical polypoid adenomyoma is composed of benign endometrial glands and a benign-appearing smooth muscle stroma, whereas the atypical polypoid adenomyoma is characterized by complex atypical endometrial glands and a cellular mitotically active smooth muscle stroma.[2,4,5]

From the Departments of *Radiology and †Pathology, Nishi-Kobe Medical Center, Kobe; and ‡Department of Radiology, Kobe University Graduate School of Medicine, Kobe, Japan.

Received for publication May 18, 2006; accepted July 14, 2006.

Reprints: Kazuhiro Kitajima, MD, 5-7-1 Koujidai, Nishi-ku, Kobe, Hyogo 651-2273 Japan (e-mail: kazu10041976@yahoo.co.jp).

Previous studies have focused on the histopathologic and imaging features of atypical polypoid adenomyomas because they have often been confused with malignant tumors. Typical polypoid adenomyomas have not received as much attention in the literature. Although there are some articles describing the sonographic appearances of typical polypoid adenomyoma, to our knowledge, magnetic resonance imaging (MRI) descriptions of this rare benign tumor have been limited. The purpose of our case series is to present the MRI characteristics of typical polypoid adenomyoma and to correlate the imaging appearances with histopathologic findings.

MATERIALS AND METHODS

Between 1997 and 2005, preoperative magnetic resonance examination was performed in 8 patients with surgically proven uterine typical polypoid adenomyoma. For this study, our institutional review board allowed exempt retrospective review of the database of patients and waived the requirement for informed consent. The patients' age range was 38 to 64 years (mean, 48.6 years). Six patients (75%) were premenopausal. Clinical presentation was hypermenorrhea in 3 patients, irregular genital bleeding in 3 patients, and dysuria and anemia in 1 patient. All the patients had no history of tamoxifen therapy. Five patients underwent simple hysterectomy, 2 patients underwent total abdominal hysterectomy with bilateral salpingo-oophorectomy, and 1 patient underwent polypectomy only. The coexistence with uterine leiomyoma was noted in 4 patients and pelvic endometriosis in 1 patient. We retrospectively reviewed the clinical records and MRI of 8 patients and correlated radiological findings with histopathologic findings. Magnetic resonance imaging was performed with a 1.5-T superconducting magnet (Magnetom Vision or Symphony; Siemens, Erlangen, Germany), using phased-array coil. The slice thickness was 6 to 8 mm, intersection gap was 1 to 2 mm, field-of-view measurements were 24 to 33 cm, and matrix size was 192 × 256 to 256 × 512. The number of signal averages was 1 to 2. Sagittal and axial T1-weighted imaging (T1WI) and T2-weighted imaging (T2WI) were obtained for all patients, and moreover, axial chemical fat-suppressed sequence (CHESS) T1WIs were obtained for 2 patients. Immediately after intravenous injection of 0.1 mmol/kg of body weight gadopentetate dimeglumine (Magnevist, Schering, Berlin, Germany), axial fat-suppression T1WIs were obtained for only 1 patient. Conventional spin-echo technique was used to obtain T1WI (repetition time range/echo time range, 600–650/10–15),

TABLE 1. Eight Patients of Typical Polypoid Adenomyoma of the Uterus

Case	Age (yr)	Size (mm)	Form	Adhered Portion	Signal Intensity on T1WIs	Signal Intensity on T2WIs
1 (Fig. 1)	52	30 × 40 × 50	Pedunculated	Posterior wall, uterine corpus	Iso	Low with high tiny foci
2 (Fig. 2)	47	20 × 24 × 25	Pedunculated	Right lateral wall, uterine corpus	Very high	Low
3 (Fig. 3)	50	10 × 20 × 35	Pedunculated	Right lateral wall, uterine fundus	Iso	High
4 (Fig. 4)	46	45 × 50 × 60	Sessile	Anterior wall, uterine corpus	Iso with high tiny foci	Low with high tiny foci
5	47	12 × 20 × 50	Pedunculated	Anterior wall, uterine corpus	Iso	Low with high tiny foci
6	64	5 × 10 × 15	Pedunculated	Anterior wall, uterine fundus	Iso	Low with high tiny foci
7	38	20 × 22 × 25	Pedunculated	Left lateral wall, uterine corpus	Iso	Iso
8	47	15 × 20 × 20	Pedunculated	Anterior wall, uterine corpus	Iso	High

and turbo spin-echo technique (3500–3800/88–100) was used for T2WI. The echo train length ranged from 5 to 10. To reduce peristalsis, 1 mL of a butylscopolamine (Buscopan; Boehringer Ingelheim, Ingelheim am Rhein, Germany) was administered intramuscularly before the examination, unless contraindicated (Table 1).

Magnetic resonance images were interpreted by 2 experienced radiologists (K.I. and Y.K.) with only the information of the pathological diagnosis of uterine typical polypoid adenomyoma; the radiologists attained consensus regarding the morphologic appearance, including the size, location, polyp's form, signal intensity, and presence of hemorrhage. The signal intensity of the lesion was identified on both T1WI and T2WI as low, isointensity, or high relative to the signal intensity of myometrium. "Very high" on T1WI indicated an intensity equal to that of fat. These radiological findings were correlated with pathological findings by 1 experienced radiologist (K.K.) and 1 experienced pathologist (K.H.).

RESULTS

On MRI, the maximum diameter of the tumors ranged from 1.5 to 6 cm (mean, 3.5 cm). The lesions were all well circumscribed. The polyp's form of the tumors were

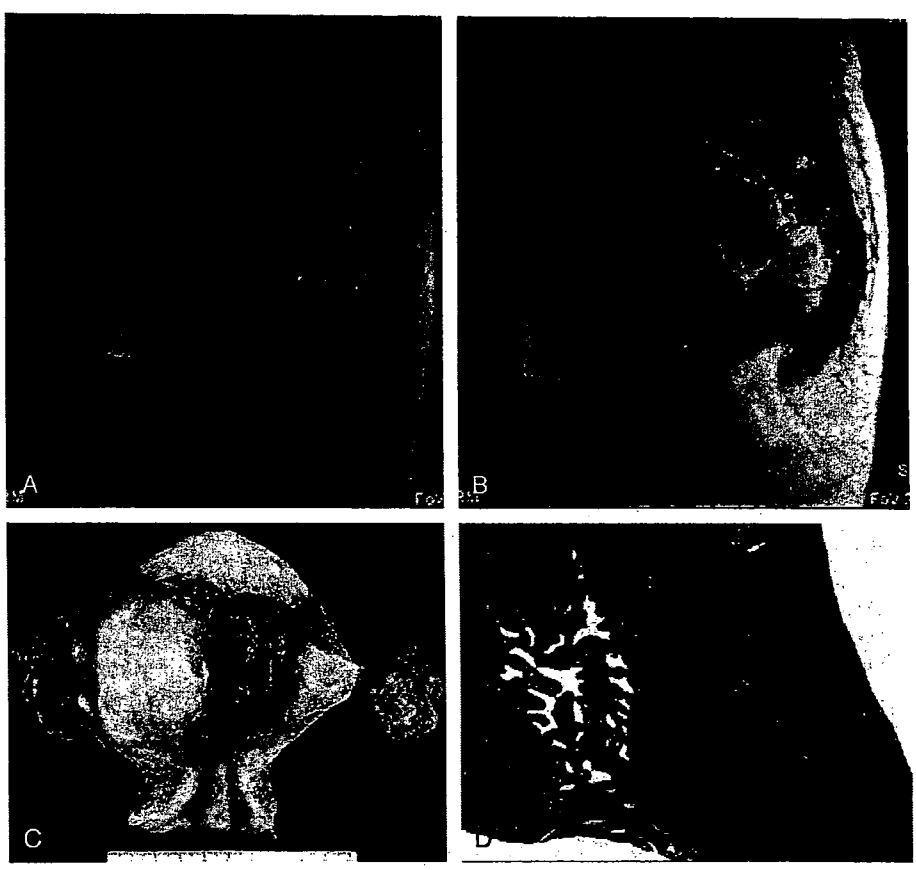

FIGURE 1. A 52-year-old woman with hypermenorrhea. A, Sagittal turbo spin-echo T2WI (repetition time/echo time = 3500/96) shows a 30 × 40 × 50-mm, well-defined pedunculated mass protruding into the cavity as hypointensity with hyperintense tiny foci relative to myometrium. B, Sagittal conventional spin-echo T1WI (650/12) shows the mass as isointensity. C, The resected specimen shows a reddish pedunculated mass adhered to the posterior wall of the uterine corpus. D, Macrograph of the resected specimen shows deeply located endometrial glands and stroma surrounded by smooth muscle.

FIGURE 2. A 47-year-old woman with hypermenorrhea. A, Axial T2WI (3600/92) shows a 20 × 24 × 25-mm, well-defined, round pedunculated mass protruding into the cavity as hypointensity. B, Axial T1WI (600/10) shows the mass as very hyperintensity. C, Fat-suppression (CHESS) T1WI does not show the signal suppression of hyperintense cystic cavity on (B) T1WI. D, The cut surface of the resected specimen shows a cystic cavity filled with bloody fluid under the endometrium of the right lateral wall of uterine corpus. E, Macrograph of the resected specimen shows focal hemorrhage within endometrial glands surrounded by smooth muscle.

pedunculated in 7 patients (Figs. 1–3) and sessile in 1 patient (Fig. 4). The adhered position of lesions was the corpus in 6 patients (Figs. 1, 2, and 4), and fundus in 2 patients (Fig. 3). On T1WI, the lesions exhibited homogeneous isointensity in 6 patients (Figs. 1 and 3), isointensity with hyperintense tiny foci in 1 patient (Fig. 4), and very high intensity in 1 patient (Fig. 2). On T2WI, the lesions exhibited hypointensity with hyperintense tiny foci in 4 patients (Fig. 1, 4), homogeneous hyperintensity in 2 patients (Fig. 3), homogeneous hypointensity in 1 patient (Fig. 2), and homogeneous isointensity in 1 patient relative to the signal intensity of myometrium. All the hyperintense areas on T1WI were not suppressed on CHESS (Figs. 2 and 4). The hyperintense area on T2WI showed contrast enhancement, as did the endometrium (Fig. 3).

Surgical and pathological records corroborated these MRI findings. Hyperintense foci on T1WI without fat suppression corresponded to hemorrhagic cavity composed of hemorrhagic endometrial tissue pathologically (Figs. 2 and 4). Hyperintense foci on T2WI reflected cystic endometrial tissue pathologically (Figs. 1 and 4). The solid portion which was isointense on T1WI and hypointense on T2WI pathologically corresponded to an admixture of smooth muscle bundles and connected tissue.

DISCUSSION

Adenomyoma (so-called focal adenomyosis) is composed of endometrial glands and stroma separated by myometrial smooth muscle, and adenomyoma which manifests as a polypoid mass protruding into the endometrial cavity is called polypoid adenomyoma. However, other studies indicate that polypoid adenomyoma may be derived from endometrial stroma cells that are capable of smooth muscle differentiation, possibly secondary to prolonged estrogenic stimulation of an endometrial stromal progenitor cell.[5–7]

On gross examination, typical polypoid adenomyomas are usually solid, well-circumscribed endometrial masses. They are usually solitary and less than 2 cm in diameter, but are sometimes larger (0.3–17 cm). The morphologic patterns of the tumors are polypoid or pedunculated and usually well demarcated from the adjacent myometrium. The tumors typically arise in the lower segment of the uterine corpus, but may involve the upper corpus or fundus. They also may arise from the endocervix and occasionally may prolapse into the vagina. Their cut surface is yellow-tan or gray to white, with a firm rubbery consistency and a lobulated smooth surface. The surface displays a trabeculated appearance that results from hypertrophied smooth muscle. They often contain several small cystic spaces of varying size, usually as large as 0.4 cm. Focal hemorrhage into the cysts or stroma may be apparent, particularly in large lesions, but calcifications are not found.[7]

This entity usually occurs in premenopausal women who are younger than those with endometrial adenocarcinoma, but rarely occurs in postmenopausal women treated with tamoxifen.[8] Abnormal vaginal bleeding is the most

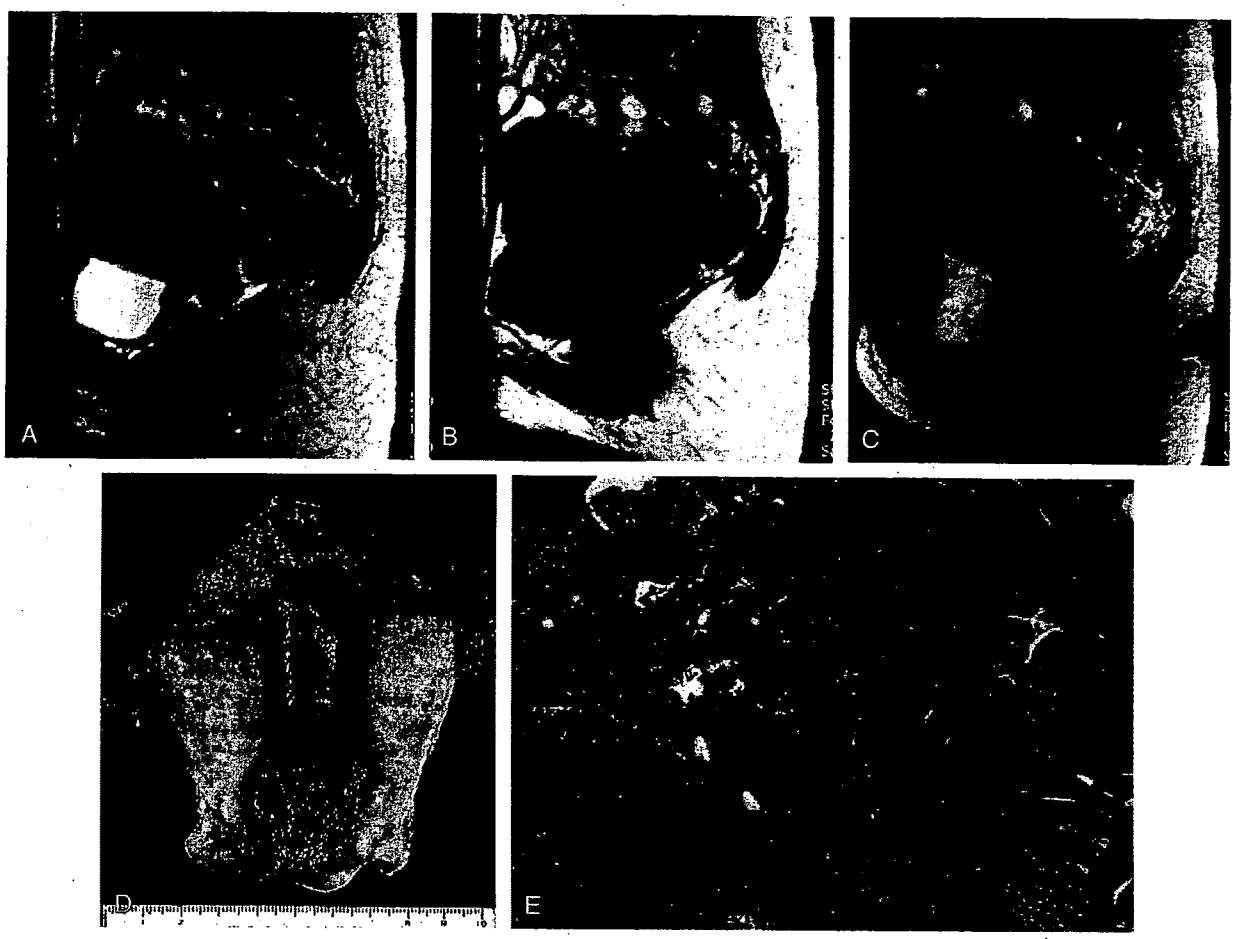

FIGURE 3. A 50-year-old woman with irregular genital bleeding. A, Sagittal T2WI (3500/96) shows a 10 × 20 × 35-mm, well-defined polypoid mass protruding into the cavity as hyperintensity. B, Sagittal T1WI (650/12) shows the mass as isointensity. C, Fat-suppression, gadolinium-enhanced sagittal T1WI shows contrast enhancement of the mass, as did the endometrium. D, The resected specimen shows a reddish polypoid mass adhered to the right lateral wall of uterine fundus. E, Macrograph of the resected specimen shows deeply located endometrial glands and stroma surrounded by smooth muscle.

common symptom, as is the case with other endometrial lesions. Other common symptoms and signs include menorrhagia, dysmenorrhea, pelvic mass, anemia, and infertility. However, these are nonspecific and can be encountered in various disorders, including more common entities such as leiomyomas and endometrial polyps. A prolapsing mass is visible at the external or is present in some cases. Polypectomy has been used successful for the definitive treatment of this entity without evidence of recurrence.[7]

There are published reports discussing the sonographic appearances of typical polypoid adenomyomas.[7,9] Ultrasound demonstrates a polypoid or pedunculated form, which has a smooth outer surface and a poorly defined margin with underlying myometrium. The solid submucosal mass may be hypoechoic or hyperechoic compared with myometrium with multiple small or large hypoechoic or hyperechoic areas, reflecting the presence of cysts or hemorrhagic areas.

Although there are only 2 reports on MRI discussing typical polypoid adenomyoma of a patient treated with tamoxifen,[9,10] to the best of our knowledge, there is no published case series, regarding the broad spectrum of MRI findings in cases of typical polypoid adenomyomas. Magnetic resonance imaging characteristics observed in our series were variable, depending on the amount of endometrial tissue, smooth muscle, and connective tissue making up the polyp. As Tamai et al[10] reported usual MRI finding of this entity, 4 (50%) of 8 patients in our series (cases 1, 4, 5, and 6) also show a circumscribed lesion which is isointense relative to the muscle with small or large hyperintense foci on T1WI or T2WI, reflecting the fascicle of smooth muscle with islands of cystic or hemorrhagic endometrial tissue (Figs. 1 and 4). Especially endometrial tissue in case 2 forms the large hemorrhagic cavity, being homogeneous hyperintensity on T1WI and hypointensity on T2WI (Fig. 2). On the other hand, there are 3 cases (cases 3, 7,

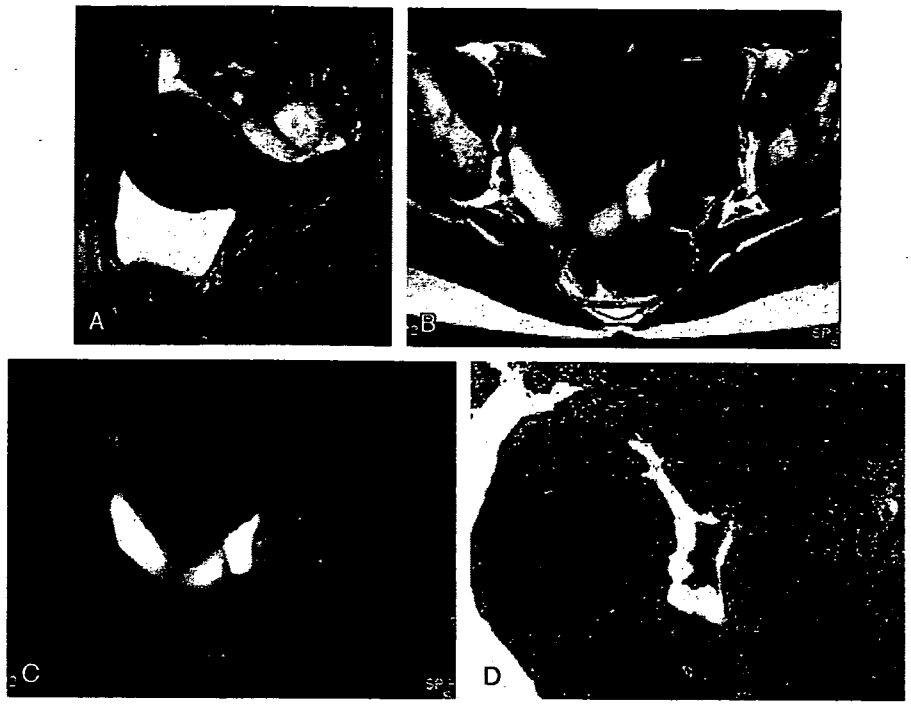

FIGURE 4. A 46-year-old woman with anemia. A, Sagittal T2WI (3500/96) shows a 45 × 50 × 60-mm, well-defined sessile mass protruding from the anterior wall of the uterine corpus into the cavity as hypointensity containing hyperintense tiny foci. B, Axial T1WI (650/12) shows the mass as isointensity with hyperintense tiny foci. C, Fat-suppression (CHESS) T1WI does not show the signal suppression of hyperintense tiny foci on (B) T1WI. D, Macrograph of the resected specimen shows focal hemorrhage within endometrial glands surrounded by smooth muscle.

and 8) that show almost homogeneous isointensity or hyperintensity related to myometrium on T2WI (Fig. 3). Unfortunately, the pathological difference between 4 usual cases (cases 1, 4, 5, and 6) and 3 unusual cases (cases 3, 7, and 8) has not been confirmed especially by 1 pathologist. Although the mass showed the homogeneous contrast enhancement in 1 case (Fig. 3), this enhancement characteristics in unusual 1 case should not be misinterpreted as being true in all cases. If magnetic resonance appearance of the mass is usual as cases 1, 2, 4, 5, and 6, it may be possible to suggest a diagnosis of typical polypoid adenomyoma preoperatively; however, in the case of unusual MRI findings, it seems impossible to distinguish a typical polypoid adenomyomas from other uterine polypoid tumors, such as endometrial polyp, degenerated submucosal leiomyoma, endometrioid carcinoma, trophoblastic disease, and mixed epithelial and mesenchymal tumors, preoperatively.[11]

Yamashita et al[12] reported the magnetic resonance appearance of 3 cases of atypical polypoid adenomyoma. As his report is almost similar to the 4 usual cases of our series (cases 1, 4, 5, and 6), the distinction between a typical polypoid adenomyoma and an atypical polypoid adenomyoma is considered to be difficult on preoperative MRI. Diagnosis of typical and atypical polypoid adenomyoma remains very difficult and until now has usually depended on the results of pathological examination.

Our study has 2 main limitations. First, it includes a small number of cases and only 1 case using gadolinium. Second, it lacks a more consistent MRI protocol, especially use of gadolinium to assess enhancement characteristics.

CONCLUSION

When there is a well-defined polypoid mass protrusion into the uterine endometrial cavity that is isointense relative to the myometrium with small or large foci of high signal on T1WI or T2WI in a premenopausal woman, typical polypoid adenomyoma can be considered in the differential diagnosis.

ACKNOWLEDGMENTS

The authors thank the members of the Department of Obstetrics and Gynecology, Nishi-Kobe Medical Center, especially Yasuihito Takeuchi and Kazuaki Katayama for their sincere cooperation.

REFERENCES

1. Gilks CB, Clement PB, Hart WR, et al. Uterine adenomyomas excluding atypical polypoid adenomyomas and adenomyomas of endocervical type: a clinicopathologic study of 30 cases of an underemphasized lesion that may cause diagnostic problems with brief consideration of adenomyomas of other female genital tract sites. *Int J Gynecol Pathol.* 2000;19:195–205.
2. Clement PB, Scully RE. Uterine tumors with mixed epithelial an mesenchymal elements. *Semin Diagn Pathol.* 1998;5:199–222.

3. Nasu K, Sugano T, Miyakawa I. Adenomyomatous polyp of the uterus. *Int J Gynecol Obstet.* 1995;48:319–321.
4. Gilks CB, Young RH, Clement PB, et al. Benign endocervical adenomyomas and adenoma malignum. *Mod Pathol.* 1996;9: 220–224.
5. Longacre TA, Chung MH, Rouse RV, et al. Atypical polypoid adenomyofibromas (atypical polypoid adenomyomas) of the uterus: a clinicopathologic study of 55 cases. *Am J Surg Pathol.* 1996;20:1–20.
6. Mazur MT. Atypical polypoid adenomyomas of the endometrium. *Am J Surg Pathol.* 1981;5:473–482.
7. Lee EJ, Han JH, Ryu HS. Polypoid adenomyomas: sonohysterographic and color Doppler findings with histopathologic correlation. *J Ultrasound Med.* 2004;23:1421–1429.
8. Takeuchi M, Matsuzaki K, Uehara H, et al. A case of adenomyomatous polyp of the uterus associated with tamoxifen therapy. *Radiat Med.* 2005;23(6):432–434.
9. Jorizzo JR, Riccio GJ, Chen MYM, et al. Sonohysterography: the next step in the evaluation of the abnormal endometrium. *Radiographics.* 1999;19:117–130.
10. Tamai K, Togashi K, Ito T, et al. MR imaging findings of adenomyosis: correlation with histopathologic features and diagnostic pitfalls. *Radiographics.* 2005;25(1):21–40.
11. Grasel RP, Outwater EK, Siegelman ES, et al. Endometrial polyps: MR imaging features and distinction from endometrial carcinoma. *Radiology.* 2000;214:47–52.
12. Yamashita Y, Torashima M, Hatanaka Y, et al. MR imaging of atypical polypoid adenomyoma. *Comput Med Imaging Graph.* 1995;19: 351–355.

JOURNAL OF MAGNETIC RESONANCE IMAGING 25:517–526 (2007)

Original Research

Anatomical and Metabolic Assessment of Prostate Using a 3-Tesla MR Scanner With a Custom-Made External Transceive Coil: Healthy Volunteer Study

Yasushi Kaji, MD,[1–3] Kagayaki Kuroda, PhD,[3,4] Takaki Maeda, MD,[1] Yuri Kitamura, MD,[1] Toshitaka Fujiwara, MD,[5] Yuichiro Matsuoka, PhD,[3] Mitsuru Tamura, PE,[6] Naoyuki Takei, PhD,[7] Tsuyoshi Matsuda, RT,[7] and Kazuro Sugimura, MD[1]

Purpose: To examine the possibility of using a 3 Tesla (T) magnetic resonance (MR) scanner with a custom-made external coil to obtain ductal details of the prostate, high-quality spectra, and metabolite mapping corresponding to prostate zonal anatomy in healthy volunteers.

Materials and Methods: MRI and two-dimensional (2D) chemical shift imaging (CSI) were performed in 16 healthy volunteers using a 3T scanner with a custom-made external transmit-receive (transceive) coil. Visualization of the prostatic duct-like structure was analyzed on T2-weighted (T2W) images. The resolution of the metabolite peaks and the distribution of metabolites in CSI were also assessed.

Results: In the axial plane, 3-mm-thick images were better than 4-mm-thick images with the same voxel volume for assessing duct-like structures and prostatic urethra. Differentiation between inner and outer citrate (Cit) peaks was frequently observed (29 out of 30). The mean peak area ratio of choline (Cho) plus creatine (Cr) over Cit in the peripheral zone (PZ) was significantly lower than in the transition zone (TZ) ($P = 0.014$).

Conclusion: 3T MR examinations of the prostate using an external coil allow information to be collected about the details of duct-like structures, the high-quality spectra of Cit, and the zone-specific distribution of metabolites.

Key Words: 3 Tesla; MR spectroscopy; MR coils; prostate; citrate

J. Magn. Reson. Imaging 2007;25:517–526.

DETECTION OF PROSTATE CANCER, especially in its early stages, is increasing due to serum prostate specific antigen (PSA) screening and systematic prostate biopsy (1). It has been reported that early T1c cancer tends to distribute in the anterior part of the apex and midgland prostate (2), and awareness of the importance of assessing the whole prostate (both the peripheral zone (PZ) and transition zone (TZ)) is increasing as a result.

MRI with an endorectal surface coil is a useful modality for staging prostate cancer (3); however, false results may occur in differentiating cancer from benign changes (4–7). Proton MR spectroscopy (MRS) of the prostate can diagnose prostate cancer in the PZ based on citrate (Cit) and choline (Cho) levels using an endorectal surface coil (8–10), but the voxel volume and spatial resolution are not sufficient to diagnose small prostate cancers.

A strong magnetic field strength scanner (≥3T) can improve the signal-to-noise ratio (SNR) and thus provide better spectral resolution compared to a 1.5T clinical scanner. Two recent studies of prostate MRI using a 3T endorectal surface coil have been reported (11,12). Prostate MRI and MRS using an external coil at high magnetic field strength is also expected to have greater efficacy than the conventional 1.5T scanner with an external coil. There is only one report in the literature about 3T MRI and single-voxel spectroscopy of the prostate using an external coil, and little has been reported about the anatomical structure of the prostate and the characteristics of prostate metabolites (13).

In this study we assessed the ability of a 3T scanner with a custom-made external coil to provide ductal details of prostate structures, high-quality spectra, and

[1]Department of Radiology, Kobe University, Graduate School of Medicine, Kobe, Japan.
[2]Department of Radiology, Dokkyo Medical University, School of Medicine, Mibu, Japan.
[3]Department of Image-Based Medicine, Institute of Biomedical Research and Innovation, Kobe, Japan.
[4]Department of Human and Information Sciences, Faculty of Information and Electronics, Tokai University, Hiratsuka, Japan.
[5]Department of Radiology, Kyoto University, Graduate School of Medicine, Kyoto, Japan.
[6]Tamura Artistic Research, Tokyo, Japan.
[7]GE Yokogawa Medical Systems, Tokyo, Japan.

Contract grant sponsor: New Energy and Industrial Technology Development Organization (NEDO), Japan; Contract grant number: 1999-2003.
Presented at the 11th Annual Meeting of ISMRM, Toronto, Canada, 2003.

Address reprint requests to: Y.K., Department of Radiology, Dokkyo Medical University, School of Medicine, 880 Kita-kobayashi, Mibu, Tochigi 321-0293, Japan. E-mail: ykaji@dokkyomed.ac.jp

Received August 16, 2005; Accepted September 27, 2006.
DOI 10.1002/jmri.20829
Published online 5 February 2007 in Wiley InterScience (www.interscience.wiley.com).

metabolite maps corresponding to prostate zonal anatomy.

MATERIALS AND METHODS

This study was approved by our institutional review board (IRB).

Subjects

The study included 16 healthy male volunteers ranging in age from 22 to 53 years (mean = 37 years), with a mean body weight of 69.6 kg. None of the subjects had any previous urologic or rectal diseases, or medication history; however, serum PSA levels were not checked in all subjects. IRB-approved informed consent was obtained from all volunteers.

MRI

In all of the subjects we obtained T1-weighted (T1W) axial images (spin-echo (SE) sequence; repetition time (TR)/echo time (TE) = 500/23 msec; field of view (FOV) = 160 × 160 mm; matrix = 512 × 256; section thickness = 4 mm; gap = 0.8 mm; number of signals acquired = 2; acquisition time = 4 minutes 16 seconds) and T2W axial images (fast spin-echo (FSE) sequence; TR/TE = 4000/92–120 msec; echo train length (ETL) = 8; FOV = 160 × 160 mm; section thickness = 3 mm (gap = 0.6 mm, matrix = 384 × 256, voxel volume = 0.78 mm^3) or 4 mm (gap = 0.6 mm, matrix = 512 × 256, voxel volume = 0.78 mm^3); number of signals acquired = 2; acquisition time = 4 minutes 16 seconds) for an adequate evaluation of the prostate, adding T2W coronal images (FSE sequence; TR/TE = 4000/92–112; ETL = 8; FOV = 160 × 160 mm; section thickness = 3 mm; gap = 0.6 mm; matrix = 384 × 256; voxel volume = 0.781 mm^3; number of signal acquired = 2; acquisition time = 4 minutes 16 seconds). To reduce the peak specific absorption ratio (SAR), we decreased the radiofrequency (RF) power to one-third and increased the pulse length threefold compared to a normal sinc-type RF pulse.

MRS

For localization of the MRS volume of interest (VOI), T2W axial images (FSE sequence; TR/TE = 3000/90; ETL = 8; FOV = 80 × 80 mm; matrix = 256 × 128; section thickness = 3 mm; gap = 0.6 mm; number of signals acquired = 2; acquisition time = 1 minute 36 seconds) were obtained. The MRS plane was positioned transversely at the midgland level (near the vermontanum). After gradient shimming and higher-order shimming were performed, we conducted proton two-dimensional point resolved spectroscopy (2D PRESS) CSI (TR/TE = 1500/145 msec; spectral width = 2016 Hz; data points = 512; FOV = 80 × 80 mm; matrix = 12 × 12: section thickness = 10 mm; voxel volume = 0.44 cm^3; number of signals acquired = 4; acquisition time = 14 minutes 31 seconds) (14). We added the spectral-spatial RF pulse for water and lipid suppression in the CSI sequence (15). The sequence was also combined with the placement of outer-volume saturation slabs to eliminate signals from periprostatic fat tissues (16).

We processed the MRS data using system software (Spectroscopy Analysis by General Electric (SAGE) and Functool, GE Medical Systems). The 2D PRESS-CSI data sets were apodized with a 2-Hz exponential function. k-Space zero-filling was not performed. The data sets were Fourier-transformed in the time domain and two spatial domains, phased, and baseline-corrected. The integral areas for the Cho (3.2 ppm), creatine (Cr, 3.0 ppm), and Cit (2.6 ppm) resonances were calculated. For quantification, the peak area ratios of Cho+Cr to Cit were calculated for each voxel (8). The metabolite ratio map was calculated and projected over the corresponding T2W image.

3T Scanner and Custom-Made External Transceive Coil

To improve the patients' comfort while maintaining a high SNR in prostate MRI and MRS, we developed a quadrature transmit-receive (transceive) pelvic coil dedicated to the prostate study at 3T (17). The custom-made coil was used with a clinical scanner (Signa VH/i 3T; GE Medical Systems, Milwaukee, WI, USA) that had a low-power (2.7 kW) RF chain for head imaging. Homogeneous excitation of the whole abdominal region was not available, and we therefore devised the transceive pelvic coil to have an RF field that was highly homogeneous around the position of the prostate, sacrificing inhomogeneity in the other regions of the FOV. The power was only 14% of that required for the abdominal coil that is commercially available in the United States (18). Our coil consists of two primary parts (as shown in Fig. 1a and b): a pair of anterior–posterior (A-P) coils sandwiching the lower abdominal part, and a pair of right–left (R-L) butterfly coils through which each thigh passes. Both the A-P and R-L elements contribute to transmission and reception. Since the angle between the superior–inferior (S-I) direction and the R or L element was 47.8°, the effective area of the R-L coil crossing the RF magnetic flux was 67% (= cos 47.8°) of the entire area surrounded by the loops. For practical scanning, each volunteer entered the deepest position of the coil with his perineum contacting the center stem in which the electrical feed point was accommodated (Fig. 1c). In order to set the prostate to an appropriate A-P position, flexible spacers were inserted at the dorsal side. The distributions of the RF field (B_1) of the coil in three orthogonal planes were calculated based on Biot-Savart's theorem (19), assuming that the electric current fed into the circuit was 1 μA.

The possibility of tissue heating by the transceive pelvic coil was examined. Temperature distribution was measured in an agar gel phantom comprised of 2% agar gel, 0.11% sodium chloride, and 0.05% sodium azide. The phantom was 200 mm in diameter and 240 mm in height, with a total weight of 7.5 kg. The phantom was placed in the coil with its side wall attached to the stem. A manual prescanning process of a single-slice (called the "scan TR") FSE sequence was used to apply RF pulses intermittently to the phantom. The parameter settings were as follows: TR/TE = 2000/17 msec; ETL

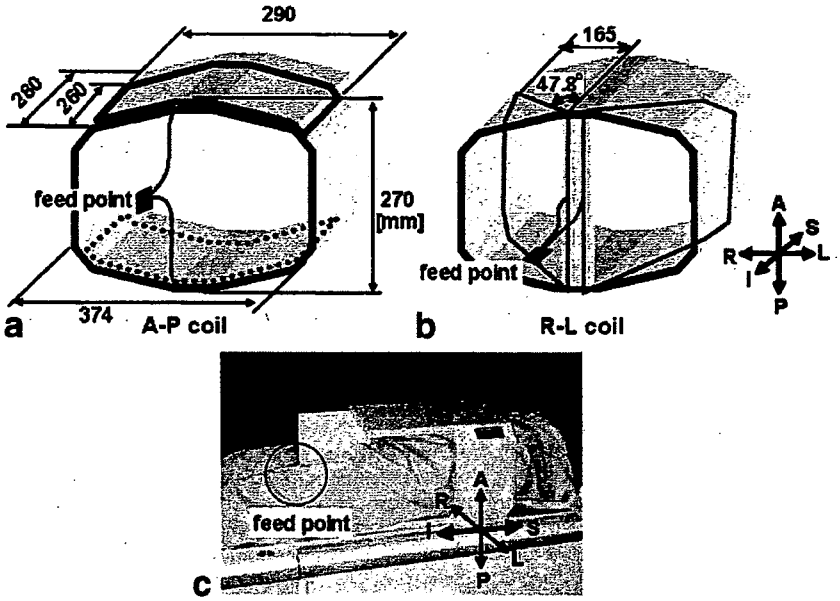

Figure 1. Overview of the custom-made transceive pelvic coil. The A-P (**a**) and R-L (**b**) coil components are shown with the electric circuit configurations and dimensions. The joint part of the R-L elements shown in b is attached to the perineum of the volunteer (**c**).

equivalent to the number of 180° pulses in a TR = 32; FOV = 240 × 240 mm; and section thickness = 10 mm. The actual RF power sampled at the output port of the power amplifier with a power meter (E4419B; Agilent Technology, Inc., Palo Alto, CA, USA), with a sampling rate of 25 msec, was averaged over the period of the intermittent excitations. The average value was 15 W. The temperature in the phantom was measured using a four-channel probe from an optical thermometer system (model 3000; Luxtron Corp., Santa Clara, CA, USA). The four channels were placed at A-P and at P = 10, 20, 30, and 40 mm. When the temperature elevation indicated by any of the channels reached 2°C, RF irradiation was stopped and the temperature distribution was imaged using a multislice phase-mapping method (20). The sliced planes were the same height as the probe channels. A spoiled gradient recalled (SPGR) acquisition in steady state sequence was used with the following parameters: TR/TE = 30/10 msec; bandwidth = 7.81 KHz, FOV = 240 × 240 mm; section thickness = 5 mm; and matrix = 256 × 128.

Data Analysis

Analysis of the Custom-Made External Transceive Coil

The B_1 field intensity was analyzed to determine the 2D contour plot in the three orthogonal planes, with a line interval of 0.1 μT/A. Temperature elevation was evaluated using both probe measurement and MRI. The probe data were plotted against the time passage to show the extent of temperature elevation under the given RF irradiation condition. The MR temperature images were calculated to show the 3D temperature elevation pattern. After we compensated for magnetic field drift by deducing the phase change in the oil bottles placed around the phantom, we obtained the phase difference between the complex images before and after the temperature change (20) at coronal slices at different heights. The phase difference maps were then converted to temperature elevation maps assuming a temperature coefficient of −0.01 ppm/°C (20).

Description of SNR on T2W Images

The SNRs of the PZ, TZ, and central zone (CZ) were calculated on T2W axial images. Because the small FOV was filled with tissue signals, we could not measure the signal intensity of the background. We used the mean of the standard deviation (SD) of the bilateral internal obturator muscles in place of the background signal, as follows:

$$\text{SNR} = (\text{signal intensity of region})/(\text{mean SD of bilateral internal obturator muscles}) \quad (1)$$

The SNR of the PZ was calculated in six midgland portion sites (right-anterior, right-middle, right-posterior, left-anterior, left-middle, and left-posterior) with circular regions of interest (ROIs) with an area larger than 50 mm^2. The SNR of the TZ was also calculated with circular ROIs ≥ 75 mm^2 in the midgland portion. The SNR of the CZ was calculated at the base portion, bilaterally. The circular ROI was larger than 8 mm^2. A paired t-test was used to determine whether the SNR of each zone at 3-mm thickness was different from that at 4-mm thickness with same voxel volume. A *P*-value of less than 0.05 was considered statistically significant.

Structural Assessment of T2W Images

We assessed whether the T2W axial and coronal images obtained at 3T could visualize the prostatic architecture, especially the small prostatic ducts, ejaculatory ducts, prostatic urethra, and sphincteric urethra (also known as the membranous urethra (21)). On T2W axial images (4 mm thick with a 512 × 256 matrix, and 3 mm

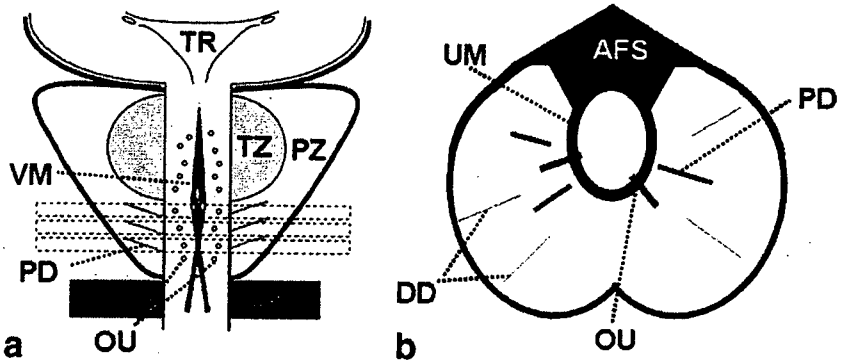

Figure 2. Prostatic ducts and urethra. **a:** Illustration of prostatic urethra and ducts in coronal view. The prostatic ducts of the PZ drain to the distal prostatic urethra, below the verumontanum. The three dotted rectangles are the slice position for the axial assessment of ducts. VM, verumontanum; PD, proximal duct-like structure in PZ; OU, ductal orifice to urethra; LA, lavatory ani muscle; TR, trigone of bladder. **b:** Axial assessment of the duct-like structure of the prostate below the midgland level. When the distal or proximal duct-like structure is more than one-third the thickness of the PZ, we interpret it as visualized. Also, when the proximal duct-like structure penetrates the muscular layer of distal prostate urethra, we take it as the opening duct into the distal prostatic urethra. AFS, anterior fibromuscular stroma; M, muscular layer of distal prostate urethra; DD, distal duct-like structure; PD, proximal duct-like structure; OU, ductal orifice to urethra.

thick with a 384 × 256 matrix), the mucosal/submucosal layer and muscular layer differentiation of proximal and distal prostatic urethra, intraductal content-muscular layer differentiation of bilateral ejaculatory ducts were assessed. A sign test was used to determine whether the layer differentiations at 3-mm thickness differed from those with the same voxel volume at 4-mm thickness. A *P*-value of less than 0.05 was considered statistically significant.

McNeal (22) described the ducts of the PZ drain as being exclusive to the distal prostatic urethra, in two vertical lines along the posterolateral urethral wall (Fig. 2). On T2W axial images (4-mm and 3-mm thickness) a mean number of distal duct-like structures in the PZ, mean number of proximal duct-like structures in the PZ, and mean number of opening ducts into the urethra were assessed every three continuous slices descending from the midgland level (Fig. 2). When the distal or proximal duct-like structure was longer than one-third of the A-P thickness of the PZ, we assessed it as visualized. Also, when the proximal duct-like structure penetrated the urethral muscular layer, we took it as the opening duct into the distal prostatic urethra. On T2W coronal images (3 mm thick), we similarly assessed duct-like structures every three continuous slices backwards from the distal prostatic urethra. A paired t-test was used to determine whether visualization of the 3-mm-thick duct-like structures differed from that of the 4-mm thick structures. We also compared 3-mm-thick axial images and 3-mm-thick coronal images with regard to visualization of ductal structures using a paired t-test. A *P*-value of less than 0.05 was considered statistically significant. The mucosal/submucosal layers, muscular layer differentiation, and length of the sphincteric urethra were assessed on the T2W coronal images.

Comparison of the SNR of Cit in the PZ

Four peaks from the strongly coupled methylene in the Cit molecules were clearly observed in vitro (23). The two inner peaks showed different phases compared to the two outer peaks (23). It was not always possible to differentiate among the complicated four peaks in the in vivo study due to the phase variation of each peak and the magnetic field inhomogeneity. We measured the Cit peak height and the area under the Cit peak as examples of spectra from a phantom (Fig. 3), even if the bottom point was below the baseline. We also measured the SD of the noise peak height at 8–10 ppm in each voxel. The SNR of Cit (SNR-cit) was determined as follows:

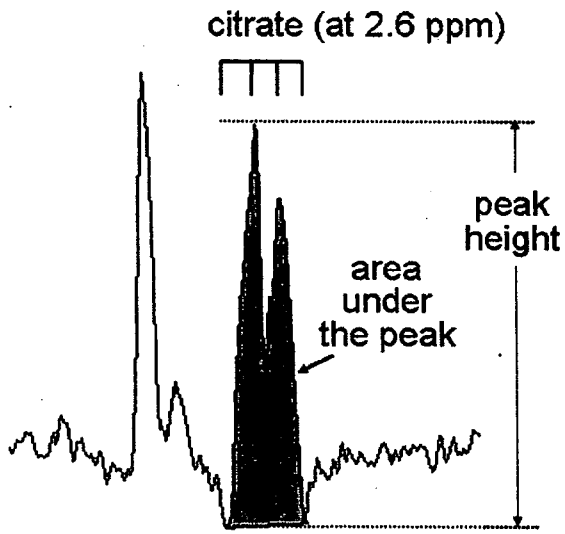

Figure 3. Measurements of the Cit quadruplet. Four peaks from the strongly coupled methylene in the Cit molecules are observed after MRS acquisition of a 30 mM-Cit-containing phantom. Because the two center peaks are different from the two outer peaks in phase, we cannot measure the height and the area under each peak accurately. We try to measure the Cit peak height and the area under the Cit peak as in the illustration, even if the bottom point is below the baseline.

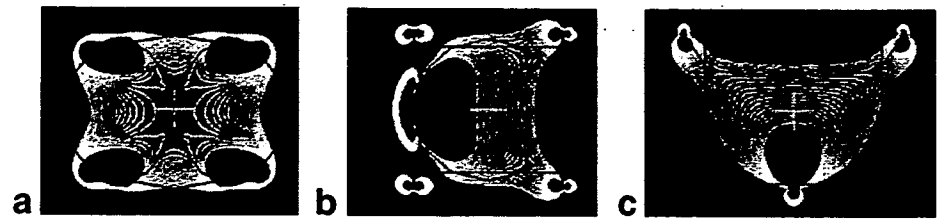

Figure 4. The distribution of the B_1 field intensity in the axial (**a**), sagittal (**b**), and coronal (**c**) planes generated by the custom-made transceive pelvic coil is shown. The highest value of the field was 4.58 μT/A. The contours were plotted for 3.0–4.5 μT/A of the field intensity with an interval of 0.1 μT/A.

SNR-cit = the peak height of citrate/
the SD of noise peak height. (2)

We selected the most anterior voxels, the middle voxels, and the most posterior voxels in the bilateral PZs on the para-midline, in which Cit peaks were clearly detected. We then measured the SNR-cit of these voxels to assess the intraprostatic spectral inhomogeneity.

Differentiation of Metabolite Peaks

In general, spectral resolution can be evaluated by linewidth measurements. However, because Cit has two inner and two outer lines, it is too difficult to measure the line width. We assessed the differentiation between the peaks by inspection bilaterally. The 32 spectra sets from 16 volunteers were evaluated for the frequency of differentiation between the inner peaks of Cit, the inner and outer peaks, the inner peaks of Cit and the polyamine peak, and the Cr peak and the Cho peak.

Peak Area Ratios of Cho+Cr to Cit of the PZ and TZ

The peak area ratio of Cho+Cr to Cit in each voxel was calculated after the data were processed. We determined the metabolite ratio in the middle voxel as representative for each PZ. Because the prostatic urethra was situated toward the midline of the TZ, the metabolite ratio in the para-midline voxel was determined as representative for the TZ. When the TZ volume was too small to place the voxel without a prostatic urethra, the ratio of the TZ voxel containing urethral tissue was accepted as representative. An unpaired t-test was used to determine whether the ratio of the PZ was different from that of the TZ. If the population variance was not equal or similar, Welch's t-test was used. A *P*-value of less than 0.05 was considered statistically significant.

RESULTS

Analysis of the Custom-Made External Transceive Coli

The calculated result of the intensity of the B_1 field of each coil portion is shown in Fig. 4. A homogeneous field appeared around the location of prostate in each plane. The temperature elevation induced by the 88-minute RF irradiation was 1.7–2.5°C, corresponding to the temperature elevation rate of 0.019–0.027°C/minute, as shown in Fig. 5a. A temperature elevation map based on the MR measurement is shown in Fig. 5b–f. The temperature elevation was highest in the region close to the coil stem in each plane (5–7°C). Elevation in the central region was approximately one-third the highest value in each plane. These results suggest that the temperature elevation rates were from 0.058–0.084°C/minute at the feed point.

Description of SNR on T2W Images

Table 1 shows the SNR of the PZ (right-anterior, right-middle, right-posterior, left-anterior, left-middle, and left-posterior) at 4-mm thickness with a 512 × 256 matrix, and the SNR of the PZ at 3-mm thickness with a 384 × 256 matrix. The difference in the mean SNR of the bilateral PZ between the two thick slices was statistically significant ($P = 0.002$), but no significant difference was observed according to thickness in SNR in the TZ ($P = 0.990$) or CZ ($P = 0.250$), as shown in Table 1.

Structural Assessment on T2W Images

On 4-mm-thick T2W axial images, differentiation of the mucosal/submucosal layers from the muscular layer in the proximal prostatic urethra and distal prostatic urethra, and intraductal content from muscular layer in the ejaculatory duct was 93.8%, 100%, and 40.6%, respectively. At 3-mm thickness, the same evaluations were 100%, 100%, and 75.0%, respectively (Table 2). There was a significant difference between thick and thin images with regard to content-muscular layer differentiation of bilateral ejaculatory ducts ($P = 0.001$).

For T2W axial images of thin and thick slabs, and coronal images of thin slabs, the mean number of distal-duct-like structures, proximal-duct-like, and opening ducts into the urethra (per three slices) are shown in Table 3 and Fig. 6. The 3-mm axial images depicted significantly more ductal structures than the 4-mm images ($P < 0.005$).

Differentiation between the mucosal/submucosal layers and the muscular layer of the sphincteric urethra was 100% on the thin T2W coronal images. The mean length of the sphincteric urethra was observed to be 17.6 ± 2.3 mm.

Comparison of the SNR of Cit

Sufficient shimming for spectroscopic examination could not be obtained in one of the 16 volunteers due to

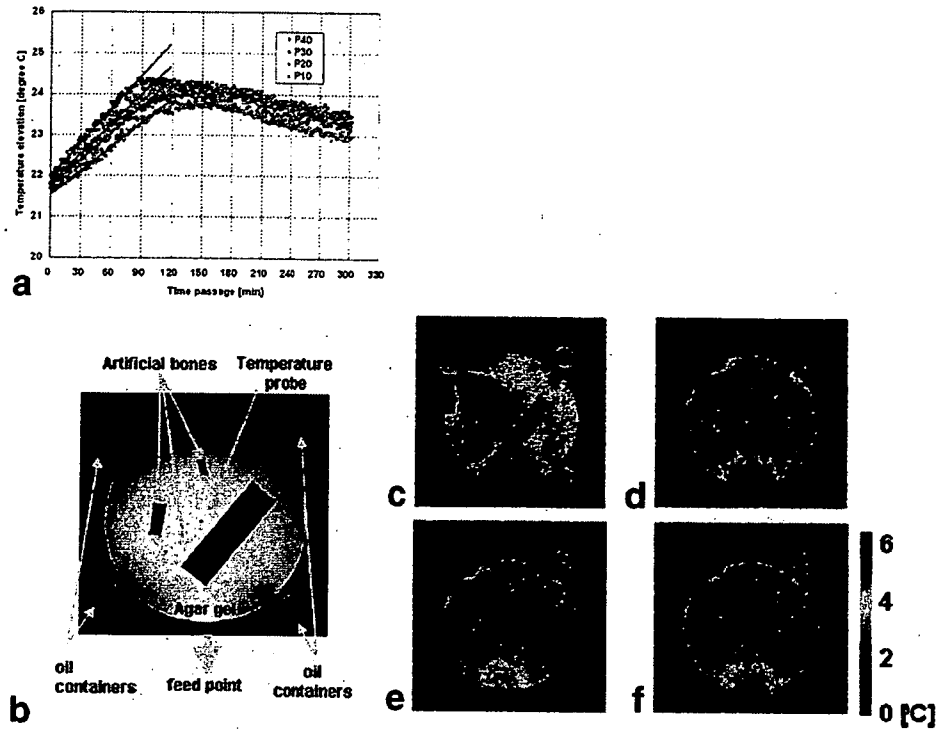

Figure 5. Measurement of temperature elevation in a phantom study. **a:** Temperature elevation measured by the optical thermometer at the center of the phantom. The four channels of the probe correspond to four different coronal cross sections (from p 10 through p 40) of the phantom. The slopes (°C/min) of the regression lines for the four channels during 88 minutes of RF irradiation were 0.0273, 0.0242, 0.0217, and 0.0193, respectively. The correlation coefficients were 0.994, 0.983, 0.982, and 0.988, respectively. **b:** The experimental setup used to examine the temperature elevation distribution in an agar gel phantom. The resultant temperature elevation distribution was obtained with 88 minutes of successive irradiation of a series of FSE RF pulses with the following parameters: TR/TE = 2000 msec/17 msec; ETL = 32; FOV = 240 × 240 mm; section thickness = 10 mm. The average irradiation power monitored by the power monitor on the scanner was 15 W. The temperature elevation images (**c–f**) were obtained at coronal planes of P10, P20, P30, and P40 immediately after the RF irradiation was stopped. The acquisitions used an SPGR with the following parameters: TR/TE = 30 msec/10 msec; bandwidth = 7.81 KHz; FOV = 240 × 240 mm; section thickness = 5 mm; matrix = 256 × 128.

rectal gas, and the data were excluded from the MRS evaluation (N = 15). The SNR-cit of the anterior, middle, and posterior voxels in the right PZ was 21.3 ± 8.7, 22.5 ± 23.4, and 20.7 ± 20.1, respectively. The SNR-cit in the left PZ was 19.0 ± 9.0, 25.6 ± 16.5, and 19.1 ± 14.6, respectively.

Differentiation of Metabolite Peaks

The frequency of differentiation between the inner peaks of Cit, the inner and outer peaks, the inner peaks of Cit and the polyamine peak, and the Cr peak and the Cho peak was 0 of 30, 29 of 30, 0 of 30, and 19 of 30, respectively, in the bilateral PZ.

Peak Area Ratios of Cho+Cr to Cit of PZ and TZ

The peak area ratio of Cho+Cr to Cit of the middle voxel in the right and left PZs was 0.36 ± 0.15 and 0.30 ± 0.15, respectively. The ratio in the TZ was 1.41 ± 1.43. The mean metabolic ratio in the bilateral PZ was significantly lower than that in the TZ (P = 0.014, Welch's t-test; Fig. 7).

Table 1
Comparison of SNR in Different Section Thickness Images*

	Right peripheral zone			Left peripheral zone			Bilateral peripheral Zone		Bilateral transition zone		Bilateral central zone	
	Anterior	Middle	Posterior	Anterior	Middle	Posterior						
4 mm thickness with 512 × 256 matrix	13.1 ± 5.7	11.8 ± 4.8	11.7 ± 5.5	13.4 ± 5.6	11.2 ± 4.8	12.5 ± 5.0	12.3 ± 5.2	P=0.002	7.5 ± 2.0	N.S.	7.7 ± 2.1	N.S.
3 mm thickness with 384 × 256 matrix	11.9 ± 4.2	10.7 ± 3.5	11.2 ± 3.8	11.6 ± 3.4	11.1 ± 2.8	11.6 ± 3.9	11.4 ± 3.6		7.5 ± 1.8		7.2 ± 1.3	

*Values are mean ± SD.
N.S. = no statistical significance (P > 0.05; paired t-test).

Table 2
Visualization of Prostatic Urethra and Ejaculatory Ducts in Different Section Thickness Images

	Proximal urethra: mucosa-muscular layer differentiation		Distal urethra: mucosa-muscular layer differentiation		Bilateral ejaculatory duct: content-muscular layer differentiation	
4 mm thickness with 512 × 256 matrix	93.8%	N.S.	100%	N.S.	40.6%	$P = 0.001$
3 mm thickness with 384 × 256 matrix	100%		100%		75.0%	

N.S. = no statistical significance ($P > 0.05$; sign test).

DISCUSSION

Although the power required for the custom-made transceive pelvic coil was only a fraction of that required for the abdominal body coil, the image quality was sufficient to observe the fine anatomy of the prostate, including the layer structures of the urethra and ejaculatory duct, and the duct-like structures running inside the prostate.

One of the most significant features of a higher-field scanner is the reduction of partial-volume averaging, which enabled us to obtain structural details with thin-slice sections. In theory, this should improve imaging assessment of prostate cancer (24). Accordingly, the 3-mm-thick images had better fidelity for assessing structural details than the 4-mm-thick images with the same pixel voxel volume. On the other hand, the SNR of the PZ was lower in a 3-mm-thick image than in a 4-mm-thick image. The intuitive improvement in image fidelity can be explained as follows (25): assuming a voxel of rectangular parallelepiped, where all three sides are the same length, l, the image fidelity, F, may be proportional to $l^2/3$. When the slice thickness becomes αl and a side of the voxel in the x-y plane becomes $/\alpha$, the fidelity, F', may be $\alpha l^2/(1 + \alpha + \lambda\alpha^2)$, where λ represents the degree of anisotropy in the tissue contained in the voxel volume. Thus, the ratio between the fidelities of the two cases with different though-plane thickness and in-plane sizes, but with the same volume, is as follows:

$$\frac{F'}{F} = \frac{3\alpha}{1 + \alpha + \lambda\alpha^2} \qquad (3)$$

See the Appendix for the derivation and behavior of this monotonically decaying function of l. When slice thickness changes from 4 mm to 3 mm, ($\alpha = 3/4$), the fidelity ratio becomes 1.29, 1.11, and 0.97 with λ of 0, 0.5, and 1.0, respectively. In the axial slice of the central height of the prostate, the change in tissue morphology is larger in the R-L (x) and A-P (y) directions than in the S-I (z) direction, which corresponds to the tendency of the anisotropy ratio to be <1 in these directions. Thus, fidelity is slightly better in the 3-mm image than in the 4-mm image.

The most significant feature of our coil is that the homogeneous B_1 field is designed to appear at the region covering the prostate. Therefore, the coil can serve for both RF transmission and the reception needed to obtain the signal from the prostate. The temperature elevation results from the phantom experiments were obtained using 88 minutes of repetitive 32-time RF irradiation with a two-second TR. The actual FSE or CSI acquisition used much sparser irradiation. The densest RF train in the present study was accompanied by T2W FSE, and was nine times per four seconds lasting for eight minutes. The total RF power in this case was about 1/40 that of the sequence used for the phantom heating experiment. This means that the temperature elevation can be estimated as 0.0021°C/min at the feed point, assuming that the relationship between RF density and the temperature elevation rate is linear. In 10-minute imaging, the temperature elevation will be 0.021°C. Since this calculation is based on results obtained for the 7.5-kg phantom with no perfusion, the elevation should be smaller and within the range of physiological deviation in an adult human body with blood circulation. In fact, no volunteer in the present study reported pain or heat in the perineum. Based on these observations, the new transceive coil was judged to be sufficiently safe for human studies.

This study is the first to visually assess the anatomical details of the prostate using a 3T scanner with an external coil. Although one report about 3T MRI and MRS with an external coil has been published, it dealt

Table 3
Visualization of Prostatic Duct-like Structures in Different Section Thickness Images

		Numbers of distal duct-like structures in peripheral zone		Numbers of proximal duct-like structures in peripheral zone		Numbers of opening duct into urethra	
T2-weighted axial images	4 mm thickness with 512 × 256 matrix	4.5 ± 5.7	$P = 0.0003$	3.8 ± 3.4	$P = 0.003$	2.8 ± 2.0	$P = 0.0001$
T2-weighted axial images	3 mm thickness with 384 × 256 matrix	8.1 ± 4.1	$P = 0.0007$	5.4 ± 3.6	$P = 0.0007$ (N.S.)	5.6 ± 3.0	$P = 0.03$
T2-weighted coronal images	3 mm thickness with 384 × 256 matrix	6.1 ± 5.2		4.5 ± 3.2		4.1 ± 2.6	

*Values are mean ± SD.
N.S. = no statistical significance ($P > 0.05$; paired t-test)

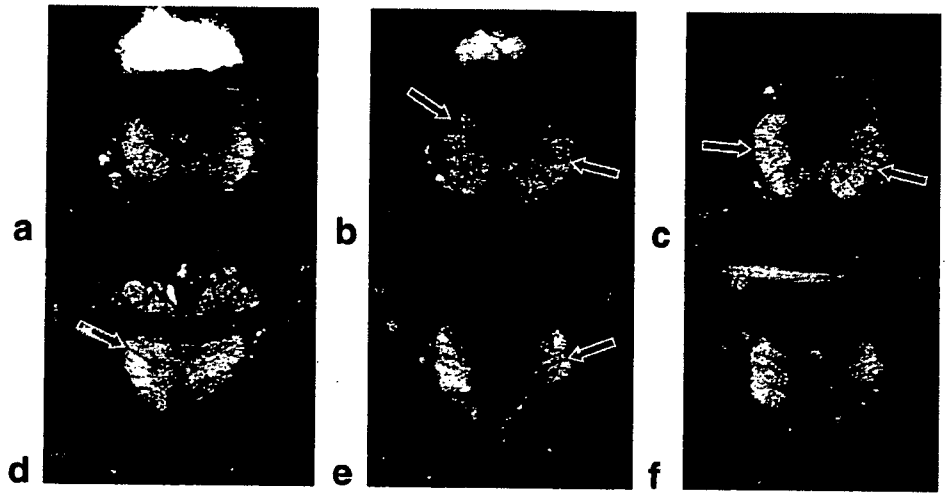

Figure 6. Images (3 mm thick) of prostatic duct-like structures in a 45-year-old volunteer. **a–c:** T2W FSE axial image (TR/TE = 4000 msec/112 msec; section thickness = 3 mm; gap = 0.6 mm; FOV = 160 × 160 mm). **d–f:** T2W FSE coronal image (TR/TE = 4000 msec/112 msec; section thickness = 3 mm; gap = 0.6 mm; FOV = 160 × 160 mm). Distal thin duct-like structures (open arrows) and proximal thick duct-like structures (solid arrows) are clearly visualized in the PZ. Furthermore, proximal duct-like structures penetrate the muscular layer of the prostatic urethra (arrowheads), which could account for the prostatic duct opening to the urethra.

mainly with the coil technology, and contained few anatomical evaluations (13). Some studies obtained high-resolution images of the prostate using an endorectal surface coil with a 1.5T clinical scanner, but the images did not reveal the details of ductal anatomy (3,26). Based on our results, 3T MRI can be used to precisely evaluate the prostate, and thus aid in the accurate detection and early diagnosis of prostate cancer while preventing signal intensity from destroying the structural details. 3T MRI may also aid in the accurate evaluation of tumor extension and staging. Evaluation of the sphincteric urethra is very important because it closely relates to the postoperative rate of incontinence and risks of positive margins (27). If 3T MRI can help us to understand the exact anatomical relationship between the prostate and the sphincteric urethra, therapy selection may be adjusted accordingly.

When proton MRS is performed on a higher-field scanner, the main advantages over 1.5T imaging are the increased SNR and improved spectral resolution. Hence, in the current study, a higher SNR spectrum and the quadruplet nature of Cit were visualized in vivo, even with CSI. Kim et al's (13) 3T study employed single-voxel techniques, while we used CSI for its greater spatial information. The Cit peak was higher in the PZ than in the TZ, and the SNR-cit in the PZ positively correlated with age. These findings are consistent with a previous study by Lowry et al (28). In addition, the peak area ratios of Cho+Cr to Cit of the TZ were lower than that of the PZ at 1.5T, as previously found in a study using an endorectal surface coil (8). The differing ratio values between the 1.5T examination and our results could be explained by the difference in J modulation of Cit in the different fields, the difficulty of measuring Cit (as described in Materials and Methods), and SNR differences of the coils.

It is necessary to keep in mind that some problems are associated with using a 3T scanner, including increased susceptibility effects from air in the bowels and hemorrhage in the prostate, increased chemical shift artifacts, and increased SAR. Magnetic field inhomogeneity depletes the quality of the spectrum in particular.

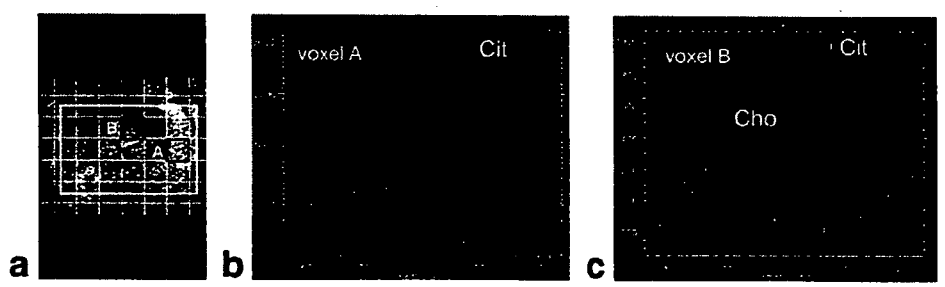

Figure 7. MR images and spectra of the prostate of a 48-year-old volunteer. **a:** T2W FSE axial image (TR/TE = 3000 msec/90 msec; section thickness = 3 mm; gap = 0.6 mm; FOV = 80 × 80 mm) for MRS localization. Voxel A is placed in the PZ, and voxel B is in the TZ. **b:** Spectrum of voxel A in the PZ (proton 2D-PRESS CSI (TR/TE = 1500 msec/145 msec; voxel volume = 0.44 cm^3). The Cit peak is extremely high. **c:** Spectrum of voxel B in the TZ (same as b). The Cit peak is also higher than the Cho peak in the TZ; however, the difference between the Cit peak height and the Cho peak height is smaller than the difference in the PZ.

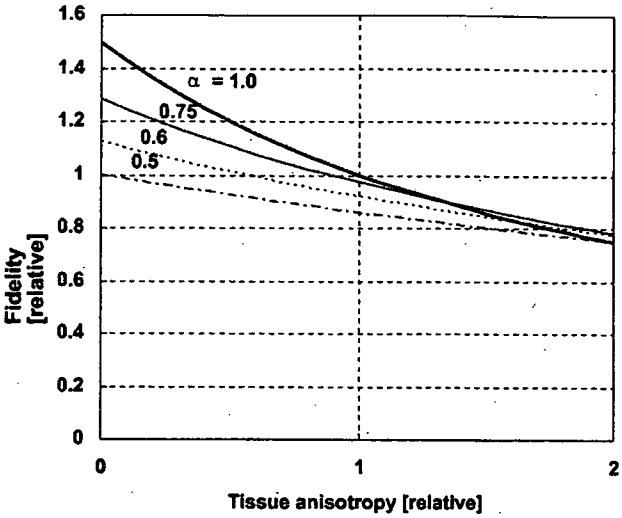

Figure 8. Relationships between the tissue anisotropy and the image fidelity for various ratios between an in-plane side length and thickness of a voxel.

Ideally, MR examinations at 3T should be performed before prostate biopsy in order to avoid susceptibility effects. In patients who experienced post-biopsy hemorrhage, we performed rigorous shimming in the area without hemorrhage and obtained suboptimal data from part of prostate. Also, the examination should be performed after defecation, with a purgative used to decrease rectal gas. For prostate imaging assessment, axial images must include slices from the seminal vesicles to the prostate apex; however, SAR restricts the number of slices that can be obtained using MRI. This may imply that optimal RF transmission power is limited in order to avoid SAR elevation, so changes of pulse sequence design are needed for reduction of RF deposition. The coronal images in this study were very useful for observing intraprostatic ductal structures and sphincteric urethra with reduced SAR, because coronal imaging of the prostate requires fewer slices than axial imaging. The development of a more efficient transceive RF coil system would allow the collection of many slices, regardless of SAR restrictions. In addition, if the SNR of Cit becomes higher, the voxel volume of CSI could be reduced. This may allow for more accurate evaluation of the distribution of metabolite ratios in the tumor, and contribute to both biopsy and radiotherapy planning.

Prostate MR examinations using 3T enabled us to obtain detailed ductal information, high-quality spectra of Cit, and specific metabolite distribution in the prostate, even when we used the custom-made external coil. In patients with rectal disease or patients who cannot tolerate the discomfort of insertion of an endorectal surface coil, 3T MRI with an external coil can help elucidate prostate ductal structures and metabolite changes.

APPENDIX

Derivation of Eq. [3]

Assuming that each voxel is a rectangular parallelepiped, and the three sides (l_x, l_y, l_z) of the parallelepiped are all in the same length, l, for simplicity, the fidelity may be defined as (29):

$$F = \frac{l_x \cdot l_y \cdot l_z}{l_x + l_y + l_z} = \frac{l^2}{3} \qquad \text{(A1)}$$

When the slice thickness, l_z, becomes α times as large as the original, and a side of the voxel in the x-y plane, l_x, becomes α-folds of the original to maintain the same voxel volume as in the present study, the fidelity may change as below:

$$F' = \frac{l/\alpha \cdot l \cdot \alpha l}{l/\alpha + l + \lambda \alpha l} = \frac{\alpha l^2}{1 + \alpha + \lambda \alpha^2} \qquad \text{(A2)}$$

where λ represents the degree of anisotropy (i.e., the ratio of the in-plane and through-plane complexities of the morphological structure of the tissue). The ratio of F' to F is calculated as:

$$\frac{F'}{F} = \frac{3\alpha}{1 + \alpha + \lambda \alpha^2} \qquad \text{(A3)}$$

This is a monotonically decaying function of λ, as shown in Fig. 8. When the slice thickness changes from 4 mm to 3 mm, for instance, α is equal to 3/4. This leads the ratio between F' and F to

$$\frac{F'}{F} = \frac{36}{9\lambda + 28} \qquad \text{(A4)}$$

REFERENCES

1. Hull GW, Rabbani F, Abbas F, Wheeler TM, Kattan MW, Scardino PT. Cancer control with radical prostatectomy alone in 1,000 consecutive patients. J Urol 2002;167:528–534.
2. Takashima R, Egawa S, Kuwao S, Baba S. Anterior distribution of stage T1c nonpalpable tumors in radical prostatectomy specimens. Urology 2002;59:692–697.
3. Hricak H, White S, Vigneron D, et al. Carcinoma of the prostate gland: MR imaging with pelvic phased-array coils versus integrated endorectal—pelvic phased-array coils. Radiology 1994;193:703–709.
4. White S, Hricak H, Forstner R, et al. Prostate cancer: effect of postbiopsy hemorrhage on interpretation of MR images. Radiology 1995;195:385–390.
5. Schiebler ML, Schall MD, Pollack HM, et al. Current role of MR imaging in the staging of adenocarcinoma of the prostate. Radiology 1993;189:339–352.
6. Schiebler ML, Tomaszewski JE, Bezzi M, et al. Prostatic carcinoma and benign prostatic hyperplasia: correlation of high-resolution MR and histopathologic findings. Radiology 1989;172:131–137.
7. Sommer FG, Nghiem HV, Herfkens R, et al. Determining the volume of prostatic carcinoma: value of MR imaging with an external-array coil. AJR Am J Roentgenol 1993;161:81–86.
8. Kurhanewicz J, Vigneron DB, Hricak H, et al. Three dimensional H-1 MR spectroscopic imaging of the in situ human prostate with high (0.24–0.7 cm^3) spatial resolution. Radiology 1996;198:795–805.
9. Kaji Y, Kurhanewicz J, Hricak H, et al. Localizing prostate cancer in the presence of postbiopsy changes on MR images: role of proton MR spectroscopic imaging. Radiology 1998;206:785–790.
10. Scheidler J, Hricak H, Vigneron DB, et al. Prostate cancer: localization with three-dimensional proton MR spectroscopic imaging—clinicopathologic study. Radiology 1999;213:473–480.
11. Futterer JJ, Scheenen TW, Huisman HJ, et al. Initial experience of 3 Tesla endorectal coil magnetic resonance imaging and 1H-spectroscopic imaging of the prostate. Invest Radiol 2004;39:671–680.

12. Bloch BN, Rofsky NM, Baroni RH, et al. 3 Tesla magnetic resonance imaging of the prostate with combined pelvic phased-array and endorectal coils: initial experience. Acad Radiol 2004;11:863–867.
13. Kim HW, Buckley DL, Peterson DM, et al. In vivo prostate magnetic resonance imaging and magnetic resonance spectroscopy at 3 Tesla using a transceive pelvic phased array coil. Invest Radiol 2003;38:443–451.
14. Duyn JH, Gillen J, Sobering G, van Zijl PCM, Moonen CTW. Multisection proton MR spectroscopic imaging. Radiology 1993;188: 277–282.
15. Schricker AA, Pauly JM, Kurhanewicz J, et al. Dual band spectral-spatial RF pulses for prostate MR spectroscopic imaging. Magn Reson Med 2001;46:1079–1087.
16. Salibi N, Brown MA. Techniques for localized spectroscopy. In: Clinical spectroscopy: first principles. New York: Wiley-Liss; 1998. p 62–105.
17. Kaji Y, Kuroda K, Matsuoka Y, et al. Rigorous shimming in prostate CSI study at 3T. In: Proceedings of the 90th Annual Meeting of RSNA, Oak Brook, IL, USA, 2004 (Abstract 735).
18. Katz-Brull R, Rofsky NM, Lenkinski RE. Breathhold abdominal and thoracic proton MR spectroscopy at 3 T. Magn Reson Med 2003; 50:461–467.
19. Boskamp EB. Fast drop off cylindrical RF transmit coils. In: Proceedings of the 10th Annual Meeting of ISMRM, Honolulu, HI, USA, 2002 (Abstract 874).
20. Ishihara Y, Calderon A, Watanabe H, et al. A precise and fast temperature mapping using water proton chemical shift. Magn Reson Med 1995;34:814–823.
21. Myers RP, Cahill DR, Devine RM, King BF. Anatomy of radical prostatectomy as defined by magnetic resonance imaging. J Urol 1998;159:2148–2158.
22. McNeal JE. Normal and pathologic anatomy of prostate. Urology 1981;17(Suppl 3):11–16.
23. Mulkern RV, Bowers JL. Density matrix calculations of AB spectra from multipulse sequences: quantum mechanics meets in vivo spectroscopy. Concepts Magn Reson 1994;6:1–23.
24. Wang Z, Bolinger L, Subramanian VH, Leigh JS. Errors of Fourier chemical-shift imaging and their corrections. J Magn Reson 1992; 92:64–72.
25. Kaji Y, Kuroda K, Maeda T, et al. Prostate phantom study for understanding characteristics of 3-tesla MRS. In: Proceedings of the 89th Annual Meeting of RSNA, Oak Brook, IL, USA, 2003 (Abstract 721).
26. Coakley FV, Hricak H. Radiologic anatomy of the prostate gland: a clinical approach. Radiol Clin North Am 2000;38:15–30.
27. Sofer M, Hamilton-Nelson KL, Schlesselman JJ, Soloway MS. Risk of positive margins and biochemical recurrence in relation to nerve-sparing radical prostatectomy. J Clin Oncol 2002;20:1853–1858.
28. Lowry M, Liney GP, Turnbull LW, et al. Quantification of citrate concentration in the prostate by proton magnetic resonance spectroscopy: zonal and age-related differences. Magn Reson Med 1996; 36:352–358.
29. Li BS, Regal J, Gonen O. SNR versus resolution in 3D 1H MRS of the human brain at high magnetic fields. Magn Reson Med 2001; 46:1049–1053.

Reprinted from

Jpn J Clin Oncol 2007;37(8)615–622
doi:10.1093/jjco/hym064

Inter-observer Variations in FDG-PET Interpretation for Cancer Screening

Akiko Suzuki[1], Yuji Nakamoto[2], Takashi Terauchi[3], Masami Kawamoto[4], Yoshihiro Okumura[5], Yutaka Suzuki[6], Toshihiko Sato[7], Nobukazu Takahashi[8], Jin Lee[8], Michio Senda[9], Kimiichi Uno[10] and Tomio Inoue[8]

[1]Department of Radiology, School of Medicine, Yokohama City University, Yokohama, [2]Department of Diagnostic Radiology, Kyoto Graduate University School of Medicine, Kyoto, [3]Research Center for Cancer Prevention and Screening, Cancer Screening Division, National Cancer Center, Tokyo, [4]Diagnostic Imaging Center, Radiology, Yuai Clinic, Yokohama, [5]Department of Radiology, PET/RI center, Okayama Kyokuto Hospital, Okayama, [6]HIMEDIC Imaging Center at Lake Yamanaka, Yamanashi, [7]Utsunomiya Central Clinic PET Center, Utsunomiya, [8]Department of Radiology, School of Medicine, Yokohama City University, Yokohama, [9]Institute of Biomedical Research and Innovation, Kobe and [10]Nishidai Clinic Diagnostic Imaging Center, Tokyo, Japan

Jpn J Clin Oncol 2007;37(8)615–622
doi:10.1093/jjco/hym064

Inter-observer Variations in FDG-PET Interpretation for Cancer Screening

Akiko Suzuki[1], Yuji Nakamoto[2], Takashi Terauchi[3], Masami Kawamoto[4], Yoshihiro Okumura[5], Yutaka Suzuki[6], Toshihiko Sato[7], Nobukazu Takahashi[8], Jin Lee[8], Michio Senda[9], Kimiichi Uno[10] and Tomio Inoue[8]

[1]Department of Radiology, School of Medicine, Yokohama City University, Yokohama, [2]Department of Diagnostic Radiology, Kyoto Graduate University School of Medicine, Kyoto, [3]Research Center for Cancer Prevention and Screening, Cancer Screening Division, National Cancer Center, Tokyo, [4]Diagnostic Imaging Center, Radiology, Yuai Clinic, Yokohama, [5]Department of Radiology, PET/RI center, Okayama Kyokuto Hospital, Okayama, [6]HIMEDIC Imaging Center at Lake Yamanaka, Yamanashi, [7]Utsunomiya Central Clinic PET Center, Utsunomiya, [8]Department of Radiology, School of Medicine, Yokohama City University, Yokohama, [9]Institute of Biomedical Research and Innovation, Kobe and [10]Nishidai Clinic Diagnostic Imaging Center, Tokyo, Japan

Received October 16, 2006; accepted March 20, 2007; published online August 18, 2007

Background: Diagnostic guidelines for the use of 2-(fluorine 18) fluoro-2 deoxy-D-glucose (FDG)-positron emission tomography (PET) in cancer screening have yet to be established. We assessed inter-observer variability in screening FDG-PET.
Methods: Subjects comprised 40 individuals who underwent FDG-PET and computed tomography (CT) for cancer screening. To assess various patterns of FDG uptakes, three subsets of the cases were selected: 'Cancer', 15 cases with cancer; 'Not malignant', 15 cases with suspected cancer by FDG-PET who were confirmed as cancer-free; and 'Normal', 10 cases without remarkable FDG uptake who were confirmed as cancer-free. A total of 68 lesions made up of malignancy ($n = 18$), benign ($n = 21$), and physiological FDG uptake ($n = 29$) were interpreted by six physicians. Each observer reviewed each case three times. Step 1 involved interpretation of PET images alone, Step 2 involved side-by-side reading of PET and CT images, and Step 3 involved re-evaluation of findings with the results of other screening tests. We assessed inter-observer agreement for each step.
Results: Inter-observer agreement for all lesions at each step was moderate, compared to fair agreement for 'Normal' subjects. Inter-observer agreement of 'Cancer' and 'Not malignant' subjects in Step 1 were better than those in Step 2 and 3; however, the differences were not statistically significant.
Conclusion: The interpretation of FDG-PET is adequately reproducible, while that of 'Normal' subjects is less reproducible. Improvement of inter-observer variability in assessing physiological FDG uptakes requires universal reporting criteria in FDG-PET. Correlative interpretation of PET, CT and other information may require standardization in subjects with suspected cancer by FDG-PET.

Key words: radiology – PET – radiology – CT/MRI – cancer screening

INTRODUCTION

2-(fluorine 18) fluoro-2 deoxy-D-glucose (FDG)-positron emission tomography (PET) plays an important role in the detection of malignant tumors, although the effectiveness of whole-body FDG-PET imaging in cancer screening remains uncertain (1,2). FDG-PET scans have been performed for cancer screening in Japan on many asymptomatic individuals who had previously never been diagnosed with cancer. FDG-PET is considered to be useful for whole-body survey because it can detect cancers of various organs that any single conventional organ-specific screening test cannot cover. High detection rates for a wide variety of cancers in cancer-screening FDG-PET has been reported by Yasuda (3)

For reprints and all correspondence: Akiko Suzuki, Department of Radiology, School of Medicine, Yokohama City University, 3–9 Fukuura, Kanazawa-ku, Yokohama, Kanagawa, 236-0004, Japan. E-mail: akiko225@yokohama-cu.ac.jp

and Chen (4); however, FDG-PET cannot be an alternative to other conventional screening tests such as physical examination, laboratory studies, mammography and thoracic computed tomography (CT), because FDG-PET analysis has obvious limitations in detecting urological cancers, cancers of low cell density, small cancers and hypometabolic or FDG-negative cancers (1,3,5). Diagnostic guidelines for the use of whole-body FDG-PET imaging in cancer screening have yet to be established. Furthermore, FDG-PET may be better interpreted with reference to CT images in cancer screening, as the determination of the precise location of FDG-avid lesions using PET alone can be challenging (6). The role of whole-body FDG-PET and CT in cancer screening is yet to be evaluated.

We surveyed a large number of cancer-screening centers in Japan in January 2005 to investigate the actual situation of cancer screening by FDG-PET. Thirty cancer-screening centers answered the questionnaire and the results were reported (data not published). The recall rate (i.e. the rate recommending diagnostic work-up due to positive findings suggesting possible cancer) varied widely from 1 to 44% betweem the centers. We hypothesized that inter-observer variation in FDG-PET interpretation for cancer screening affected clinical decisions to recommend either close examination or follow-up and caused variability in the recall rate. Inter-observer variation in FDG-PET for cancer screening is of particular interest because of the challenge involved in detecting suspected lesions, of which the incidence is very low, out of numerous cases of equivocal FDG uptake; some radiologists tend to over-diagnose FDG uptake to avoid potential false negative outcomes. Numerous investigations have shown that considerable variability exists among radiologists in the interpretation of screening tests such as mammography and thoracic CT without training or computer-aided diagnosis (7–9). This variability affects the diagnostic accuracy of screening studies and clinical decisions to recommend either close examination or follow-up. Herder et al. reported that inter-observer agreement of FDG-PET between clinical and final stage was good in patients with suspected lung cancer (10). Inter-observer agreement of interpretation in relevant focal pulmonary abnormality of FDG-PET was also reported to be good by Joshi et al. (11). To the best of our knowledge, variability in radiologists' interpretations of whole-body FDG-PET for cancer screening has yet to be examined. The purpose of the present study is to assess inter-observer variations in screening FDG-PET.

MATERIALS AND METHODS

Case Materials

FDG-PET and CT data of 40 subjects (21 male, 19 female, median age 57 years) were collected from seven cancer-screening centers in Japan and were used in this study. The scanning took place between April 2004 and March 2005; all subjects were symptom-free and underwent FDG-PET and CT on the same day for cancer screening together with other physical and laboratory tests. The 40 subjects consisted of Group 1 'Cancer', 15 true positive cases with suspected cancer by FDG-PET who were confirmed to have cancer by biopsy; Group 2 'Not malignant', 15 false positive cases with suspected cancer by FDG-PET and recommended for close examination who were confirmed as cancer-free on follow-up or biopsy; and Group 3 'Normal', 10 true negative cases who had no suspected lesion detected in FDG-PET and were confirmed to be cancer-free at 1-year follow-up. It should be noted that the number of cases in each group does not reflect the fractional occurrence of each outcome in cancer screening using FDG-PET. This study did not deal with false negative cases on PET because this is peripheral to the primary aim of assessing inter-observer variation in the interpretation of malignant lesions without remarkable FDG uptakes. Among the 15 'Cancer' subjects, primary disease involved the lung ($n = 3$), thyroid ($n = 3$), colon ($n = 2$), breast ($n = 2$), stomach ($n = 2$), pancreas ($n = 1$) and malignant lymphoma ($n = 2$). These cancers are commonly detected in FDG-PET and CT during cancer screening (1,4).

On reviewing the 40 subjects together with all the reference data, a total of 103 lesions were identified, presenting varying intensities of FDG uptake. Thirty-five of 103 lesions that were considered true negative lesions in 'Cancer' and 'Not malignant' cases were excluded because of the absence of confirmed reference data. A final total of 68 lesions were diagnosed as malignant ($n = 18$), benign ($n = 21$), or physiological FDG uptake ($n = 29$). Among the 15 'Cancer' subjects, 18 malignant lesions were detected and enrolled as true positive lesions. In the 15 'Not malignant' subjects, 13 benign lesions and five physiological uptakes were enrolled as false positive lesions. In the 10 'Normal' subjects, eight benign lesions and 24 physiological uptakes were enrolled as true negative lesions. All malignant lesions and seven benign lesions were confirmed on biopsy. At 1 year after FDG-PET, 14 benign lesions and 29 physiological uptakes were confirmed as stable or diminished in uptake. In the present study, we examine the interpretations of these 68 lesions made by each physician.

Scanning of Whole-Body PET and CT Study

FDG-PET and CT of the 40 cases were performed in seven different institutions between April 2004 and March 2005. All PET images were obtained using a standardized protocol in accordance with the FDG-PET guidelines for cancer screening issued in 2004 by the Japanese Society of Nuclear Medicine. Patients fasted for at least 5 h prior to scanning. We obtained a whole-body PET image from the head to the thigh using a PET or PET/CT scanner at 50–60 min following the injection of 300–450 MBq of FDG. Transmission images were obtained to correct for photon attenuation using a germanium-68 line source. For PET/CT, PET attenuation

correction factors were calculated from the CT images. We reconstructed image datasets using the ordered-subsets expectation maximization algorithm. We acquired a whole-body CT image from the head to the pelvis without intravenous contrast agent using a CT scanner or PET/CT scanner. The CT scanners and technical parameters were as follows: (i) Robusto (Hitachi Medico, Tokyo, Japan) multi-detector four row CT, 120 kVp, 100–160 mAs, beam pitch 1.75 and 10 mm thickness; (ii) Light Speed Ultra (GE Medical Systems, Tokyo, Japan) multi-detector eight row CT, 120 kVp, 175 mAs maximum with automatic exposure control system, 1.35 pitch and 5 mm thickness; (iii) Brilliance 16 (Philips Electronics Japan, Tokyo, Japan) multi-detector 16 row CT, 120 kVp, 150 mAs maximum with automatic exposure control system, 0.9 pitch and 5 mm thickness; (iv) Biograph LSO (Siemens-Asahi Medical Technologies, Tokyo, Japan) PET/CT with multi-detector two row CT, 130 kVp, 80 mAs maximum with automatic exposure control system, 1.15 pitch and 4 mm thickness; (v) Biograph LSO (Siemens-Asahi Medical Technologies), PET/CT with multi-detector two row CT, 130 kVp, 60 mAs, 1.5 pitch and 3 mm thickness; (vi) Eminence-SOPHIA (Shimadzu Corporation, Kyoto, Japan) helical CT, 120 kVp, 187.5 mAs, 1.4 pitch and 7 mm thickness; (vii) CT-Turbo (Hitachi Medico) helical CT, 120 kVp, 100–120 mAs, and 5–10 mm thickness. The mAs settings were selected to optimize spatial and contrast resolution. Tube current modulation was used to minimize the radiation dose to the individuals.

The PET/CT images were divided into PET and CT images, which were interpreted by side-by-side reading.

Observing Radiologists

FDG-PET and CT data were interpreted by six physicians with experience in both FDG-PET and CT, but who had not previously seen the study cases. The six observers were based at the six different cancer-screening centers with various recall rates from 1 to 44% [1, 10, 12, 23, 35, 44] that were mentioned in the introduction; each observer had between 4 and 10 years experience in reading screening FDG-PET.

Image Interpretation

Each observer reviewed each case in three steps. Step 1 involved interpretation of PET images alone, Step 2 involved side-by-side reading of PET and CT, and Step 3 involved re-evaluation of findings with reference to past history, smoking and drinking habits, and the results of other screening tests performed at the same time such as blood tests, fecal occult blood inspection and other imaging modalities that included magnetic resonance (MR) imaging for lower abdomen assessment and ultrasonography (US) for upper abdomen and thyroid gland assessment. In Step 2, each observer interpreted PET and CT by side-by-side reading without using fusion images. Findings of FDG uptake in each step were recorded as site and score depending on the likelihood of malignancy (1–5 points: 1, definitely not malignant; 2, probably not malignant; 3, equivocal; 4, probably malignant; 5, definitely malignant).

Each observer gave a score rating for every lesion that he/she considered to represent remarkable FDG uptake in each case. We analyzed each observer's interpretation of the 68 lesions that had been identified in advance as having confirmed reference data. Any of the 68 lesions that were not recognized by the observer as remarkable FDG uptake were given a score of 1 (definitely not malignant). Any lesions that were detected other than the 68 previously mentioned were excluded from analysis because of the absence of confirmed reference data.

All images were viewed with the same software using Synapse, medical imaging and information management network system, housed at the Fujifilm's demonstration showroom in Ginza, Tokyo, Japan.

Data Analyses

We assessed observer accuracy and variation using the scores given by each observer based on the relevant lesion. Sensitivity, specificity and positive predictive value (PPV) data were calculated from the interpretations of the six observers for each step. Receiver-operating characteristic (ROC) analysis was also performed as the standard method for evaluating observer accuracy, as sensitivity and specificity offer an incomplete description of accuracy and depend on the decision threshold selected by the observer to define positive diagnoses. The area under the ROC curve (Az) was used as a summary index of accuracy. Sensitivity for malignancy was calculated as the proportion of malignancies given a rating of 3–5. Specificity was defined as the fraction of benign lesions or physiological FDG uptakes for which a rating of 1–2 was reported. Inter-observer agreement in 68 lesions on the likelihood of malignancy (1–5 points) for each step was also assessed using the κ statistic.

Statistical Analysis

The Wilcoxon matched pairs signed rank sum test was applied to the sensitivity, specificity, and PPV means for each step to test for significant differences. Values of $P < 0.05$ were considered indicative of statistically significant differences. We calculated weighted κ values to describe concordance in reporting as 'slight' (0.00–0.20), 'fair' (0.21–0.40), 'moderate' (0.41–0.60), 'substantial' (0.61–0.80), or 'almost perfect' (0.81–1.00) (12,13). We conducted all analyses using MedCalc for Windows, version 7.6.0.0 (MedCalc Software, Mariakerke, Belgium), except for ROC analysis, which was performed using the software ROCKIT (C. Metz, University of Chicago, Chicago, IL, USA). ROC software was used to fit a binormal ROC curve